

Power-optimized Stiffness and Nonlinear Position Control of an Actuator with Variable Torsion Stiffness*

P. Beckerle^{1,3}, J. Wojtusch^{2,3}, J. Schuy¹, B. Strah^{1,3} S. Rinderknecht¹ and O. v. Stryk^{2,3}

Abstract—Introducing compliant actuation to robotic joints is an approach to ensure safety in closer human-machine interaction. Further, the possibility to adjust stiffness can be beneficial, considering energy storage and the power consumption required to track certain trajectories. The subject of this paper is the stiffness and position control of the Variable Torsion Stiffness (VTS) actuator for application in compliant robotic joints. For the realization of a variable rotational stiffness, the active length of a torsional elastic element in serial configuration between drive and link is adjusted in VTS. Based on a brief repetition of this basic concept and the deduction of an extended drive train model, this paper gives an advanced power analysis clarifying power-optimal settings from previous basic models and identifying additional settings that allow for a more versatile operation. Based on these results that can be generalized to other variable elastic actuator concepts, an optimized strategy for setting stiffness is determined considering the whole system dynamics and natural frequencies as well as antiresonance effects. For position control of VTS in a prototypical implementation, a nonlinear position controller is designed by means of feedback linearization and the extended model. Adapting the stiffness of the model in the controller provides the possibility to ensure the required tracking performance although the system is modified significantly by changing the drive train stiffness. Further, notes on practical implementation and a friction compensation are given.

I. INTRODUCTION

Contemporary, the interaction of humans and robots is getting closer and thus safety aspects receive increased priority in the design of robots. A promising approach to ensure safety are compliant concepts for joint actuation in series elastic setup. Beyond safety benefits, those can provide energy storage and optimize the drive train efficiency and power consumption [1]. For such purposes, the possibility to adjust the stiffness of the compliant drive train is advantageous, as it allows to match its natural frequency to the frequency of the desired trajectory as shown in [2]–[4]. First concepts of actuators with variable stiffness like the Series Elastic Actuator (SEA) [2], [5] and the Mechanical Impedance Adjuster (MIA) [6] were introduced in the 1990s. Present concepts can be categorized in four groups of fundamental stiffness variation principles [1]: Equilibrium-controlled, antagonistic-controlled, structure-controlled and mechanically controlled

stiffness. Actuators using the equilibrium-controlled principle like SEA, change the equilibrium position of a spring as shown in [7]. Approaches working with the antagonistic-controlled principle utilize actuators coupled antagonistically and working against each other as in AMASC [8]. A high number of contemporary variable stiffness designs belong to structure-controlled and mechanically controlled solutions. While the first ones change stiffness by a modification of the physical structure of an elastic element as in MIA, the latter ones like MACCEPA [9] adjust the system stiffness by pretension. The authors' approach is based on variable torsion stiffness (VTS) and aims at biomechanically inspired robotic joints as in lower limb prostheses [10]. As the torsional joint stiffness is adjusted by varying the length of an elastic element, it belongs to the structure-controlled variable compliant actuators. The functional concept described in [10] enables compact actuators with a large stiffness bandwidth and customizable dynamic characteristics. A first simulative study based on models of drivetrain and compliance control mechanism in [10] indicated that power consumption is comparable to other present approaches for moving the link, while VTS has very low power consumption in setting joint stiffness and shows to be beneficial in retaining the selected stiffness and varying it during operation.

In this paper the stiffness and position control of VTS in the actuation of compliant robotic joints are investigated based on an advanced power analysis. After a brief repetition of the basic concept, an extended drive train model is derived based on the preliminary one in Section II. An advanced power analysis considering the parameters of a prototypical implementation is performed based on simulations of the extended model in Section III. Subsequently, Section IV gives an optimized strategy for setting the drive train's stiffness considering the system dynamics including the natural frequencies as well as antiresonance effects. In Section V, a position control algorithm for practical application in the VTS prototype is implemented by feedback linearization with stiffness adaptation and simulative results showing the tracking performance are presented. After some notes on practical implementation of this control scheme, a conclusion and an outlook are given in Section VI.

II. MODELING

The concept and functional units of an actuator using variable torsion stiffness are given in the upper part of Figure 1, while the lower part shows the control schemes presented in Section IV and V. In the VTS concept, actuator 1 applies a torque τ_i to the torsional elastic element and

*This work was funded by Forum for Interdisciplinary Research of Technische Universität Darmstadt.

¹ Institute for Mechatronic Systems, Department of Mechanical Engineering, Technische Universität Darmstadt, lastname@ims.tu-darmstadt.de

² Simulation, Systems Optimization, and Robotics Group, Department of Computer Science, Technische Universität Darmstadt, lastname@sim.tu-darmstadt.de

³ Member, IEEE

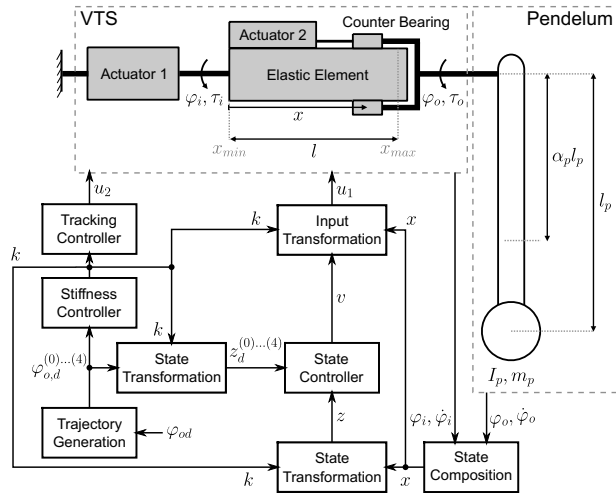


Fig. 1. Principle of VTS functionality and block diagram of control architecture.

thus moves the link. The adjustment of the torsional drive train stiffness $k_{vts}(x)$ is implemented by varying effective length x of the elastic element via the location of a counter bearing using actuator 2. Due to the separation of the actuators driving the joint and setting its stiffness, this adjustment is conducted independently from the control of joint position in idle state as well as during operation.

A. Basic Models

The main transfer paths of actuators with variable torsion stiffness are the compliant drive train and the stiffness control path. Models for both parts are derived in [10]. The model of the compliant drive train is given by

$$\tau_t = k_{vts}(x) \vartheta = \frac{G I_t(x)}{x} (\varphi_o - \varphi_i). \quad (1)$$

In (1), the torsional angle ϑ corresponding to the difference of the output position φ_o and the input position φ_i is induced by the torsional torque τ_t of the elastic element, which is equal to $-\tau_o$ in Figure 1. The torsional stiffness $k_{vts}(x)$ of the elastic element is described based on the material's modulus of elasticity in shear G , the active length x of the elastic element and the torsional moment of inertia $I_t(x)$ of the elastic element. Considering frictional effects in the counter bearing, the stiffness control path is modelled by

$$F_f = -\mu \frac{k_{vts}(x)}{r_n} \vartheta . \quad (2)$$

B. Extended Drive Train Model

In [10] the model of the elastic drive train is used for the simulation of driving a pendulum via the VTS concept. The dynamic equation of this system is given by

$$I_{rp} \ddot{\varphi}_o + m_p g \alpha l_p \sin(\varphi_o) = -\tau_t = \tau_o. \quad (3)$$

Yet, this model assumes an ideal actuator without inertia and hence neglects the dynamic influences of it. In this paper, this preliminary model is thus extended regarding the mechanical

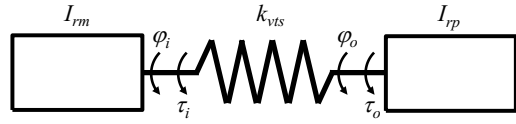


Fig. 2. Extended mechanical model of the VTS drive train.

transfer behaviour of actuator 1 as shown in Figure 2 and in [11]. Hence, the dynamic equations of the system are

$$M(q_o) \ddot{q}_o + C(\dot{q}_o, q) + G(q_o) + K(q_o - q_i) = 0, \quad (4)$$

$$J \ddot{q}_i - K(q_o - q_i) = \tau_i, \quad (5)$$

according to the model for elastic joint robots from [12]. In this, $q_o = \varphi_o$ represents the position of the output or link sided pendulum and $q_i = \varphi_i$ corresponds to the input or drive sided position. The input torque τ_i equals the actuator torque τ_m transformed by the gear ratio i_g . In (5), the matrices $M(q_o) = I_{rp}$, $C(\dot{q}_o, q_o) = 0$, $G(q_o) = m_p g \alpha_p l_p \sin(\varphi_o)$, $J = I_{rm}$ and $K = k_{vts}$ represent scalar values, since only one link is considered. Regarding the link side, the moment of inertia of the pendulum is given as $I_{rp} = m_p (\alpha_p l_p)^2 + I_p$. The reduced inertia $I_{rm} = i_g^2 I_m + I_g + I_c$ of actuator, transmission and coupling regarding the drive side is considered in J according to [13]. In $G(q_o)$ the gravitational terms are modeled, while K represents the elasticity of the drive train. All mechanical parameters of the model are based on the prototype given in [14] and presented in Table I.

TABLE I
PARAMETERS OF MECHANICAL SETUP AND CONTROL [10], [15].

	Parameter	Value	Unit
VTS drive train	k_{vts}	$50 - 350$	Nm/rad
	x_{min}	$10.0 \cdot 10^{-3}$	m
	x_{max}	$100.0 \cdot 10^{-3}$	m
	I_m	$1.80 \cdot 10^{-4}$	$kg\ m^2$
	I_g	$0.95 \cdot 10^{-4}$	$kg\ m^2$
	I_c	$2.40 \cdot 10^{-3}$	$kg\ m^2$
Pendulum	i_g	80	
	m_p	6.81	kg
	I_p	$11.05 \cdot 10^{-2}$	$kg\ m^2$
	l_p	0.45	m
	α_p	0.77	
	g	9.81	$m\ s^{-2}$
Control	$k_{R,p}$	10000	$Nm\ rad^{-1}$
	$k_{R,v}$	4000	$Nm\ s^{-1}\ rad^{-1}$
	$k_{R,a}$	600	$Nm\ s^{-2}\ rad^{-1}$
	$k_{R,j}$	40	$Nm\ s^{-3}\ rad^{-1}$
	a	5.9	Nm
	b	357.1	$Nm\ s\ rad^{-1}$

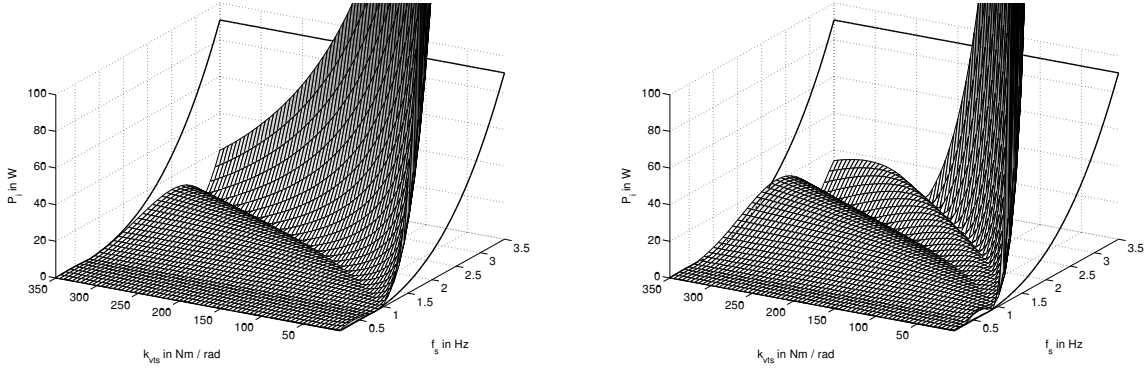


Fig. 3. Power consumptions $P_{m,i}$ of an ideal stiff actuator (black line), the basic VTS model (shaded mesh, left) and the extended VTS model (shaded mesh, right) versus frequency f_s and stiffness k_{vts} .

III. POWER ANALYSIS

For the power analysis of the drive train, the powers required to perform the motion of input $P_{m,i} = \tau_i \dot{\varphi}_i$ and output $P_{m,o} = \tau_o \dot{\varphi}_o$ are investigated based on (5) and $\tau_o = -\tau_t$. Additionally, the power consumed for stiffness setting is analyzed with (2). As in [10], stiffness adjustment is presumed to happen instantaneously and the setting energy E_s is given by

$$E_s = \int_{x_1}^{x_2} |F_f| dx, \\ = \left| \mu \frac{\tau_t}{R} (x_2 - x_1) \right|. \quad (6)$$

In this radial distance of the counter bearing r_n is assumed to equal to the outer radius R and the elastic element is supposed to have a neglectable damping constant c_{vts} [10]. The motion energies of input and output are further given by $E_{m,i} = \int_{t_m} |P_{m,i}| dt$ and $E_{m,o} = \int_{t_m} |P_{m,o}| dt$. Thus, the average power consumption P_i , required from the actuators, results from the total energy consumption $E_i = E_{m,i} + E_s$ for link motion and stiffness adjustment divided by the elapsed time t_m .

The investigations of the extended model are performed by an inverse dynamics simulation of (5) considering a sinusoidal trajectory with a magnitude of 10° . As the power consumption for an ideal stiff actuator equals $P_{m,o}$, it is also derived from this simulation. For comparability to [4] and [10], the calculations for the basic drive train model 1 are repeated with inverse dynamics. Further, the initial energy of the different models is considered in all simulations, since this represents the actual operational state and is compatible with the assumptions in the studies mentioned above. In contrast to those, the investigated stiffness interval is extended to range from 5 Nm/rad up to 350 Nm/rad, while frequencies from 0.1 Hz to 3.5 Hz are considered to clarify the system dynamic influences of the extended model. Further, the usage of inverse dynamics allows to avoid the necessity to consider settling times or falsifying influences due to the control algorithm.

A. Link Motion

The power consumption required for motion resulting from the two simulations are given in Figure 3. In both plots, the power consumption of an ideal stiff actuator is indicated by a black line on the axes planes for reference, while the shaded meshes in both plots represent the power consumptions of the VTS drive train. The results for the basic model shown in the left plot coincide with the ones from [10], as one area of minimum power consumption can be identified. Comparing this and the results for other compliant actuators in [4] to the right plot showing the results from the extended model, it becomes distinct that two regions of minimum power consumption occur instead of one. This is due to the system dynamics of the extended model that considers the input inertia I_{rm} caused by actuator, coupling and transmission. With the increased investigated frequency range, a further area of minimum power consumption can be observed at a frequency below 0.5 Hz. In contrast to the other minimum areas, this one is influenced by the variation of the stiffness k_{vts} only weakly. As the extended model describes the system dynamics better than the preliminary ones, one can see that a deeper investigation of the extended model as in Section IV is required to find a strategy for setting power-optimized stiffness values.

B. Stiffness Setting

As the model for the stiffness adjustment path of VTS is not extended, it shows comparable power requirements for both simulation and is thus presented for the extended model only. The power consumption is determined by

$$P_s = \frac{E_s}{t_m}. \quad (7)$$

In [10] it is shown, that the power required for stiffness adjustment is very low in comparison to the power demand of link motion. Hence, the results from the simulation with the extended model are given by absolute power instead of relative energy values in figure 4. Again, the low power consumption of the stiffness adjustment can be observed.

It also becomes obvious that the required powers increase with decreasing stiffness due to the characteristics of the elastic element. Beyond this, the power consumption reaches a minimum at about 0.8 Hz for low stiffness values. This is due to the low input power required at this point and the resulting low values for the friction force F_f on the counter bearing.

IV. STIFFNESS CONTROL

With the insights from power analysis, an power-optimized strategy for adjusting the stiffness of the drive train can be derived. In Figure 1, this strategy corresponds to the block stiffness controller that determines the power-optimized stiffness value based on the model and the current trajectory. For basic models considering the output inertia I_{rp} only, minimum power consumption could be achieved by matching the natural frequency of the linearized system to the frequency of the trajectory due to [4] and [10]. In the case of VTS and the corresponding basic model this is given by

$$\omega_{0,b} = \sqrt{\frac{k_{vts} + m_p g l_p \alpha_p}{I_{rp}}}, \quad (8)$$

regarding the operating point $\varphi_o = 0^\circ$. Due to the results from the analysis of the extended model this is not sufficient, since three areas of minimum power consumption occur instead of one. To investigate the causes of these areas, the system dynamics of the extended model are analyzed. First indications on stiffness setting due to the system dynamics of the drive train are given in [11] based on the linearized extended model. Yet, the two natural frequencies examined there do not explain the power consumption observed in Figure 3 completely and hence further investigation is necessary. For this, the transfer function from the input torque τ_i to the output position q_o

$$\frac{q_o(s)}{\tau_i(s)} = \frac{k_{vts}}{c_4 s^4 + c_2 s^2 + c_0}, \quad (9)$$

and the transfer function from the input torque τ_i to the input position q_i

$$\frac{q_i(s)}{\tau_i(s)} = \frac{I_{rp} s^2 + k_{vts} + m_p g l_p \alpha_p}{c_4 s^4 + c_2 s^2 + c_0}, \quad (10)$$

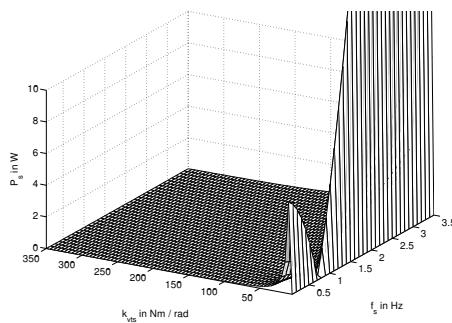


Fig. 4. Absolute power consumption P_s for setting stiffness in the extended VTS model (shaded mesh, right) versus frequency f_s and stiffness k_{vts} .

of the linearized extended model are considered, where

$$c_4 = I_{rp} I_{rm}, \quad (11)$$

$$c_2 = (I_{rm} + I_{rp}) k_{vts} + I_{rm} m_p g l_p \alpha_p, \quad (12)$$

$$c_0 = k_{vts} m_p g l_p \alpha_p, \quad (13)$$

and $\varphi_o = 0^\circ$ is chosen as operating point. For both transfer functions the system characteristics represented by the natural frequencies are identical and given by the roots of the denominator $c_4 s^4 + c_2 s^2 + c_0$.

Further, an antiresonance can be observed due to the zero of the transfer function from the input torque τ_i to the input position q_i . The frequency $\omega_{a,e}$ of this antiresonance is identical to the natural frequency $\omega_{0,b}$ of the basic model given in (8) and thus only depends on the output characteristics. In Figure 5 the variation of the natural and antiresonance frequencies of the linearized system are plotted in comparison to the contour of the motion power consumption determined with the extended model. The comparison of the contour from nonlinear simulation shows, that the frequencies determined from linearized transfer functions represent an appropriate approximation of the nonlinear ones. Further, the comparison of the frequencies and the power contour in Figure 5 clarify the reasons of the power-optimal areas distinctly: The first natural frequency $\omega_{0,e1}$ is about 0.5 Hz and influenced by stiffness variation only slightly. Due to this and the low power requirements at low frequencies, tuning the drive train to this frequency should not lead to significant improvements compared to ideal stiff operation of VTS. Selecting stiffness by considering the other two areas of minimum power consumptions shows to be a more appropriate method, as those can be manipulated better by stiffness adjustment, provide significant decrease of power consumption and cover the investigated frequency range. As shown in Figure 5, these areas are caused by the antiresonance observed at the input with $\omega_{a,e}$ and the second natural frequency $\omega_{0,e2}$ of the system. With this clarification of the reasons leading to the power minima, one can see that setting stiffness by (8) based on basic models as in [4] and [10],

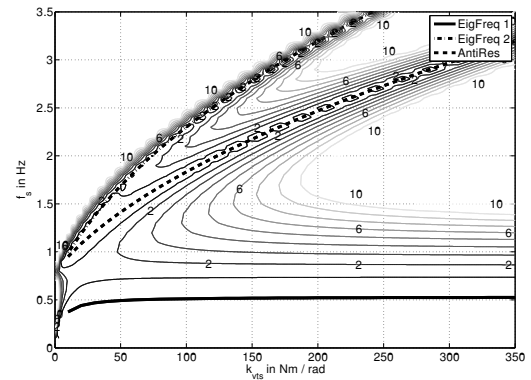


Fig. 5. Linearized natural frequencies and anti-resonance versus stiffness k_{vts} in comparison to power contour.

leads to strategies that are power-optimized. Although such models do not consider the system dynamics of the drive train completely, making the natural frequency $\omega_{0,b}$ of the basic model is power-optimal, since this frequency is identical with the antiresonance $\omega_{a,e}$ of the extended model. Thus, stiffness adjustment is performed using

$$k_{vts,a}(\omega) = -I_{rp}\omega^2 - m_p g l_p \alpha_p, \quad (14)$$

Anyhow, the stiffness adjustment can be optimized further based on the second natural frequency $\omega_{0,e1}$ of the extended model resulting in the adjustment law

$$k_{vts,02}(\omega) = -\frac{I_{rm} I_{rp} \omega^4 + I_{rm} m_p g l_p \alpha_p \omega^2}{(I_{rp} + I_{rm}) \omega^2 + m_p g l_p \alpha_p}. \quad (15)$$

Since it is more sensitive to stiffness variation, this allows to cover an even wider range of frequencies during operation. Additionally, it becomes possible to tune the drive train based on the second natural or the antiresonance frequency depending on the current application scenario. For this, switching between these areas frequently should be avoided, as this would increase power consumption.

V. POSITION CONTROL

For position control of the extended model, the computed torque control from [10] is replaced by a controller based on feedback linearization as proposed in [12], [16]. Further, the influence of varying the stiffness k_{vts} is investigated and notes on practical implementation are given subsequently.

A. Feedback Linearization

For the design of the feedback linearization control scheme that is depicted by the block diagram in Figure 1, the extended model (5) is rewritten in nonlinear state space representation with the state vector

$$[x_1 \ x_2 \ x_3 \ x_4]^T = [q_o \ \dot{q}_o \ q_i \ \dot{q}_i]^T. \quad (16)$$

Hence, the system is represented by

$$\dot{x} = f(x) + g(x) u, \quad (17)$$

$$\dot{x} = \begin{bmatrix} x_2 \\ \frac{m_p g \alpha_p l_p}{I_{rp}} \sin(x_1) - \frac{k_{vts}}{I_{rp}} (x_1 - x_3) \\ x_4 \\ \frac{k_{vts}}{I_{rm}} (x_2 - x_4) \end{bmatrix} + \begin{bmatrix} 0 \\ 0 \\ 0 \\ \frac{1}{I_{rm}} \end{bmatrix} u,$$

where the system input u equals the input torque τ_i . Instead of using a nonlinear control law directly, this torque is computed by a linear controller $v(z)$ after performing feedback linearization by the state transformation

$$z = \begin{bmatrix} x_1 \\ x_2 \\ -\frac{m_p g \alpha_p l_p}{I_{rp}} \sin(x_1) - \frac{k_{vts}}{I_{rp}} (x_1 - x_3) \\ -\frac{m_p g \alpha_p l_p}{I_{rp}} x_2 \cos(x_1) - \frac{k_{vts}}{I_{rp}} (x_2 - x_4) \end{bmatrix}, \quad (18)$$

and the input transformation

$$u(x, z) = \frac{I_{rp} I_{rm}}{k_{vts}} (v(z) - a(x)), \quad (19)$$

based on the nonlinear function

$$a(x) = \frac{m_p g \alpha_p l_p}{I_{rp}} \sin \left[x_2^2 + \frac{m_p g \alpha_p l_p}{I_{rp}} \cos(x_1) \frac{k_{vts}}{I_{rp}} \right] + \frac{k_{vts}}{I_{rp}} (x_1 - x_3) \left[\frac{k_{vts}}{I_{rp}} + \frac{k_{vts}}{I_{rm}} + \frac{m_p g \alpha_p l_p}{I_{rp}} \cos(x_1) \right], \quad (20)$$

due to the design given in [12], [16]. Assuming that the model fits the real system perfectly, the system with the two transformations behaves like a linear state space system with

$$A = \begin{bmatrix} 0 & 1 & 0 & 0 \\ 0 & 0 & 1 & 0 \\ 0 & 0 & 0 & 1 \\ 0 & 0 & 0 & 0 \end{bmatrix}, \quad (21)$$

and $B = [0 \ 0 \ 0 \ 1]^T$, while the components of transformed state vector z correspond to the output position φ_o , velocity $\dot{\varphi}_o$, acceleration $\ddot{\varphi}_o$ and jerk $\dddot{\varphi}_o$. For this system, a linear tracking control law

$$v(z) = z_d^{(4)} + k_R \tilde{z}, \quad (22)$$

is designed. In this, $z_d^{(4)}$ corresponds to the desired value of the fourth derivative of the transformed state $z_1 = q_1$, \tilde{z} is the state control error and $k_R = [k_{R,p} \ k_{R,v} \ k_{R,a} \ k_{R,j}]$ are the control gains determined by pole placement of all poles to -10 as given Table I.

B. Influence of Stiffness Adjustment

For the adaptation of the control algorithm according to the modification of the drive train stiffness during operation, this is considered in the model based transformations as shown in the block diagram in Figure 1. By adapting the input and state transformations given in 19 and 18 to the current stiffness, feedback linearization and the suitability of the linear control design should be guaranteed for all possible stiffness values.

To investigate this and the dynamical errors occurring due to stiffness modification, the controlled extended model is simulated considering a sinusoidal reference trajectory with 2.0 Hz and a magnitude of 10° . During the simulation time, the stiffness k_{vts} is modified from 160 Nm/rad to 60 Nm/rad, which is implemented by a fifth order polynomial. The results from this simulation are shown in Figure 6. In the upper left plot, the angular positions are depicted, while the lower left plot presents the corresponding control errors. It becomes distinct, that both errors increase due to the dynamical changes during stiffness modification. Anyhow, a stable control with robust performance regarding stiffness variation is provided, as both control errors are compensated in a short period of time. In the upper right plot of 6, the trajectory of stiffness modification is shown and the power-optimized values are marked: The dotted line corresponds to a stiffness of 123.41 Nm/rad representing an adjustment of the drive train according to the antiresonance frequency with (14). Further, the dash-dotted line indicates tuning the drive train by considering the second natural frequency with (15) and thus selecting a stiffness of 73.59 Nm/rad.

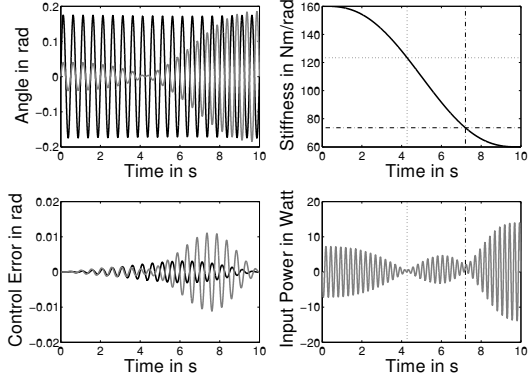


Fig. 6. Simulation results of the controlled extended model: Left plots - Position and control error of input (grey) and output (black). Upper right plot - Stiffness modification. Lower right plot - Input power consumption.

The indications of those values, are also given in the lower right plot, that represents the required input power and shows a significant reduction for those.

C. Notes on Practical Implementation

For practical implementation on the test rig shown in [14], the assumption that the model ideally fits the real system might not be given. Hence, the control algorithm should be extended to be robust against model deviations as it is done in [12] for example. Further, the sensor minimal solution given there could be used to control the test rig by measuring the input position φ_i and velocity $\dot{\varphi}_i$ only. Due to friction in the motor-gear unit of the prototype setup, the position control is extended by a friction compensation as shown in [14]. This is introduced to the control law $\tau_i = u(x, z) + \tau_{fr,i}$ by feedforward control $\tau_{fr,i} = a \text{sign}(\dot{\varphi}_i) + b \dot{\varphi}_i$, where the model parameters in Table I are identified by least squares regression based on measured data.

VI. CONCLUSIONS

With the extended model of VTS given in Section II, holistic power analysis of the mechanical drive train system is performed in Section III. The results show that three areas of power-optimized operation can be found due to the two natural frequencies and the antiresonance of the drive train. With this, a basis for the selection of power-optimized stiffness values for specific applications and trajectories is given. Furhter, the low energetic effort for setting energy shown in [10] is substantiated. Based on those results, the causes of areas with low power consumption requirements are clarified by the system dynamics and tuning laws for power-optimized stiffness adjustment are given in Section IV. Beyond this, feedback linearization is applied to the extended model and adapted regarding the stiffness selection in Section V. A simulation shows that appropriate tracking performance can be provided depending on the rate of stiffness adjustment. Additionally, modifying the stiffness in a range containing both power-optimized values shows their positive effect in

dynamic operation. For the prototype, notes on practical control and friction compensation are shown in V.

In their future works, the authors will focus on the implementation and control of the VTS prototype. This comprises the robust control of the drive train as well as the automation and control of the counter bearing for stiffness adjustment. Further, a optimization of the elastic elements will be conducted for better integration and structural integrity. With the finalized prototype, the results from simulations will be compared to experimental investigations.

ACKNOWLEDGMENT

The authors thank Bühler Motor GmbH and National Instruments Germany for hardware donations.

REFERENCES

- [1] R. Van Ham, T. G. Sugar, B. Vanderborght, K. W. Hollander, and D. Lefebvre, "Compliant Actuator Designs Review of Actuators with Passive Adjustable Compliance/Controllable Stiffness for Robotic Applications," *IEEE Robotics & Automation Magazine*, vol. 16, pp. 81–94, 2009.
- [2] G. A. Pratt and M. M. Williamson, "Series elastic actuators," in *Proceedings of the 1995 IEEE/RSJ International Conference on Intelligent Robots and Systems*, 1995.
- [3] S. Klug, T. Lens, O. von Stryk, B. Möhl, and A. Karguth, "Biologically inspired robot manipulator for new applications in automation engineering," in *Proc. of Robotik 2008*, 2008.
- [4] B. Vanderborght, R. Van Ham, D. Lefebvre, T. G. Sugar, and K. W. Hollander, "Comparison of Mechanical Design and Energy Consumption of Adaptable, Passive-compliant Actuators," *The International Journal of Robotics Research*, vol. 28, pp. 90–103, 2009.
- [5] M. M. Williamson, "Series elastic actuators," Master Thesis, Massachusetts Institute of Technology, 1995. [Online]. Available: <http://mit.dspace.org/handle/1721.1/6776>
- [6] T. Morita and S. Sugano, "Design and development of a new robot joint using a mechanical impedance adjuster," in *1995 IEEE International Conference on Robotics and Automation*, 1995.
- [7] K. W. Hollander, R. Ilg, T. G. Sugar, and D. Herring, "An efficient robotic tendon for gait assistance," *Journal of Biomechanical Engineering*, vol. 128, pp. 788 – 791, 2006.
- [8] J. W. Hurst, J. E. Chestnutt, and A. A. Rizzi, "An actuator with physically variable stiffness for highly dynamic legged locomotion," in *2004 IEEE International Conference on Robotics and Automation*, 2004.
- [9] B. Vanderborght, N. G. Tsagarakis, R. Ham, I. Thorson, and D. G. Caldwell, "MACCEPA 2.0: compliant actuator used for energy efficient hopping robot Chobino1D," *Autonomous Robots*, vol. 31, pp. 55–65, 2011.
- [10] J. Schuy, P. Beckerle, J. Wojtusch, S. Rinderknecht, and O. von Stryk, "Conception and Evaluation of a Novel Variable Torsion Stiffness for Biomechanical Applications," in *IEEE International Conference on Biomedical Robotics and Biomechatronics*, 2012.
- [11] P. Beckerle, J. Wojtusch, S. Rinderknecht, and O. v. Stryk, "Mechanical influences on the design of actuators with variable stiffness (accepted)," in *6th International Symposium on Adaptive Motion of Animals and Machines*, 2013.
- [12] A. W. Spong, "Modeling and control of elastic joint robots," *Journal of Dynamic Systems, Measurement, and Control*, vol. 109, pp. 310–318, 1987.
- [13] D. Gross, W. Hauger, J. Schröder, and W. A. Wall, *Technische Mechanik 3: Kinetik*. Springer, 2010.
- [14] P. Beckerle, F. Stuhlenmiller, J. Schuy, J. Wojtusch, S. Rinderknecht, and O. v. Stryk, "Friction compensation and stiffness evaluation on a variable torsion stiffness (accepted)," in *6th International Symposium on Adaptive Motion of Animals and Machines*, 2013.
- [15] B. Vanderborght, B. Verrelst, R. V. Ham, M. V. Damme, P. Beyl, and D. Lefebvre, "Development of a compliance controller to reduce energy consumption for bipedal robots," *IEEE Robotics & Automation Magazine*, 2009.
- [16] J.-J. E. Slotine and W. Li, *Applied Nonlinear Control*. Prentice hall Internation Inc., 1991.